The First State (S_0) in the Catalytic Cycle of the Water-Oxidizing Enzyme: Identification of a Water-Derived μ-Hydroxo Bridge, Assigned as the Slowly Exchanging Substrate

Thomas Lohmiller,*[,†] Vera Krewald,[†,¶] Arezki Sedoud,[‡,§] A. William Rutherford,[‡,§] Frank Neese,[†] Wolfgang Lubitz,[†] Dimitrios A. Pantazis,[†] and Nicholas Cox*[,†,‖]

[†]Max-Planck-Institut für Chemische Energiekonversion, Stiftstrasse 34-36, D-45470 Mülheim an der Ruhr, Germany

[‡]Department of Life Sciences, Imperial College London, London SW7 2AZ, United Kingdom

[§]iBiTec-S, URA CNRS 2096, CEA Saclay, 91191 Gif-sur-Yvette, France

[‖]Research School of Chemistry, Australian National University, Canberra, ACT 2601, Australia

Supporting Information Placeholder

ABSTRACT: Nature's water splitting catalyst, an oxygen-bridged tetra-manganese calcium (Mn_4O_5Ca) complex, sequentially activates two substrate water molecules generating molecular O_2. Its reaction cycle is composed of five intermediate (S_i) states, where the index *i* indicates the number of oxidizing equivalents stored by the cofactor. After formation of the S_4 state, the product dioxygen is released and the cofactor returns to its lowest oxidation state, S_0. Membrane-inlet mass spectrometry measurements suggest that at least one substrate is bound throughout the catalytic cycle, as the rate of ^{18}O-labeled water incorporation into the product O_2 is slow, on a millisecond to second timescale depending on the S state. Here, we demonstrate that the Mn_4O_5Ca complex poised in the S_0 state contains an exchangeable hydroxo bridge. Based on a combination of magnetic multiresonance (EPR) spectroscopies, comparison to biochemical models and theoretical calculations we assign this bridge to O5, the same bridge identified in the S_2 state as an exchangeable fully deprotonated oxo bridge [Pérez Navarro *et al. Proc. Natl. Acad. Sci. U.S.A.* **2013** *110*, 15561]. This oxygen species is the most probable candidate for the slowly-exchanging substrate water in the S_0 state. Additional measurements provide new information on the Mn ions that constitute the catalyst. A structural model for the S_0 state is proposed that is consistent with available experimental data and explains the observed evolution of water exchange kinetics in the first three states of the catalytic cycle.

1. INTRODUCTION

Nature's water splitting catalyst, an oxygen-bridged tetra-manganese calcium cofactor (Mn_4O_5Ca), is found in the transmembrane protein super-complex photosystem II (PSII).[1-8] Biological water-splitting chemistry is driven by the reaction center of PSII, a multi-chlorophyll assembly, found buried in the center of the transmembrane region. Visible-light excitation generates a charge-separated state with the electron donor ($P680^{\bullet+}$) subsequently acting as the chemical oxidant for the water splitting reaction, successively extracting electrons from the Mn_4O_5Ca cofactor.[9] $P680^{\bullet+}$ and the Mn_4O_5Ca cofactor are coupled via a redox-active tyrosine residue Y_Z (D1-Tyr161), which acts as a single electron relay.[10,11] The action of the cofactor is to accumulate the four oxidizing equivalents needed to drive the water-splitting reaction. As such it moves through a cycle of five distinct redox states that differ by one-electron oxidation, termed the S_i states (*i* = 0–4, **Fig. 1A**).[12] The release of dioxygen is followed by the spontaneous decay of the S_4 state back to the lowest (most reduced) S state, S_0. Stable regeneration of the S_0 state is thought to involve the rebinding of one substrate water based on substrate exchange data, which monitor the uptake of isotope-labeled water into the product O_2 molecule by mass spectrometry.[13,14]

The Mn_4O_5Ca cofactor, as visualized using synchrotron radiation X-ray diffraction (SR-XRD),[1] and recently using femtosecond X-ray free electron laser diffraction (XFEL),[2] adopts a distorted chair conformation with a Mn_3O_4Ca cubane unit forming the base of the chair (**Fig. 1B**). The fourth, outer Mn is attached to the base of the chair via the oxygen bridges O4 and O5. The new XFEL structure[2] displays Mn-Mn distances consistent with extended X-ray absorption fine structure (EXAFS) constraints, which was not seen in SR-XRD structures due to photochemical reduction during data collection.[15-19] The short Mn-O

distances resolved for the oxygen bridges O1-O4 support assigning these linkages as oxo (O^{2-}) bridges. In contrast, the comparatively longer Mn3/Mn4-O5 distances can be

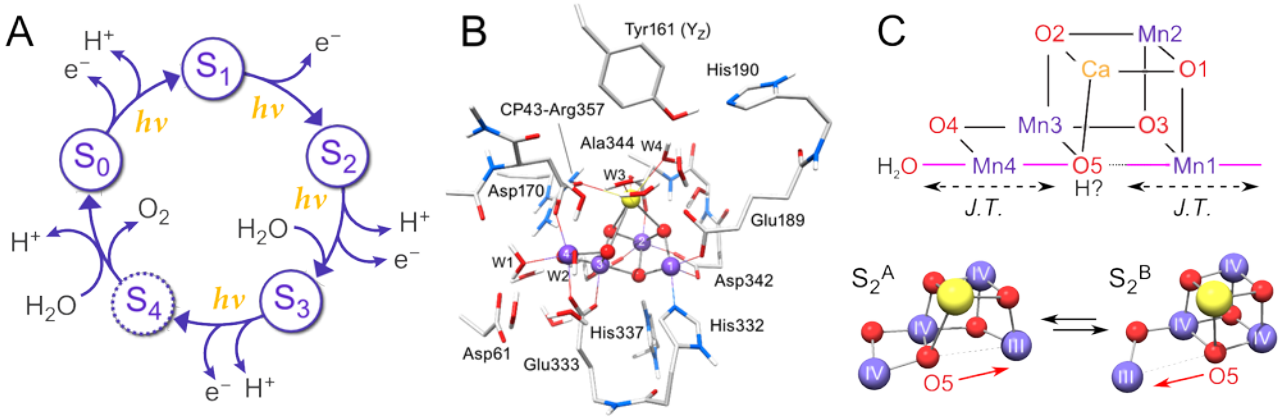

Figure 1. **(A)** Light ($h\nu$)-driven S-state cycle of the OEC indicating oxidation by $Y_Z^{\bullet}$, proton release and substrate water binding. **(B)** DFT cluster model of the OEC in the S_T = 1/2 conformation of the S_2 state including its immediate surroundings.[20] Mn ions are shown in purple, O in red, Ca in yellow, C in light grey, N in blue and H (mostly omitted for clarity) in white. **(C) Top:** Schematic representation of the inorganic Mn_4O_5Ca core in the XFEL structure including the Jahn–Teller axes (magenta bars) of $Mn1^{III}$ and $Mn4^{III}$ in the proposed S_1 state.[2] **Bottom:** The two conformational isomers of the S_2 state Mn_4O_5Ca core, differing in the connectivity of O5 and the Mn^{III} position.[20]

interpreted in terms of O5 representing either an oxo (O^{2-}) or a μ-hydroxo (OH^-) bridge. A straightforward protonation assignment, however, cannot be made as the O5 bridge sits along the Mn^{III} Jahn–Teller (JT) axis of Mn4 (and Mn1), see **Fig. 1C**.

It remains a subject of debate as to whether XFEL structures reported for the resting (S_1) state of the cofactor[2,21,22] solely represent this state. This is in part because of post-crystallization and (the lack of) pre-flash treatments that supposedly affect S-state synchronization. In case the crystals have been pre-flashed,[22] it is however not clear if the kinetics of S-state synchronization[23,24] are identical for the partially dehydrated crystal preparations used in crystallographic studies as compared to solution samples, where S-state synchronization has been studied in depth. This must be a concern as solvent water has been implicated in the proton-electron-coupled oxidation of D2-Tyr160 (Y_D).[25] It is thus conceivable that the reported XFEL structures represent an admixture of centers poised in both the S_1 and S_0 states, i.e. containing an S_0 population of ≈25% of centers. In addition, questions have been raised as to whether light atoms in the vicinity of metal atoms can be accurately determined, with the position of O5 in particular being subject to debate.[26] This further compounds the difficulty in assigning the protonation state of S_1 (and S_0) based on structural constraints.

The ambiguity with regard to the protonation state of O5 is particularly problematic for establishing the substrate's interaction with the catalyst in its resting state. O5 is a likely candidate for the first substrate water that binds to the catalyst,[27-29] with its assignment as a potential substrate site based on its structural lability: O5 displays fast exchange kinetics with solvent water,[27] and has been shown to adopt two ligand binding motifs in the S_2 state (**Fig. 1C, bottom**).[20] It has been suggested that the latter property, namely coordination flexibility, may be important for second substrate inclusion and activation of the catalyst.[6,30,31] If O5 represents a μ-hydroxo bridge in the S_1 state, then it could represent a water molecule in the S_0 state as the S_0-S_1 transition is coupled to proton release.[3,32,33] Alternative protonation assignments for O5 would instead require O5 to represent a μ-hydroxo or μ-oxo bridge in S_0, and several experimental and computational studies have considered such protonation patterns.[19,34-41] The presence of a μ-hydroxo bridge in S_0 has been suggested earlier by EXAFS based on a fitted increased Mn-Mn distance in S_0 as compared to S_1, however at a comparatively low experimental distance resolution.[42,43] In each of these scenarios, catalyst regeneration, following O_2 release, involves the binding (and deprotonation) of substrate water for the next reaction cycle.

Here we demonstrate that the Mn_4O_5Ca complex poised in the lowest S state (S_0) does indeed contain a μ-hydroxo (OH^-) bridge. With the aid of DFT calculations, new multifrequency/multiresonance EPR data are used to deduce the geometric structure of the S_0 state, constrain the local oxidation states of all four Mn ions, the bridging network (connectivity) of the cofactor and its protonation state. This study, in conjunction with published membrane-inlet mass spectrometry data, strongly supports assigning O5 as the first substrate of the biological water reaction. Consequences for product release and catalyst regeneration are discussed.

2. MATERIALS AND METHODS

2.1 PSII sample preparation. PSII core complex preparations from wild-type *Thermosynechococcus elongatus*[44] and from a mutant in which Y_D had been replaced by a phenylalanine[45] were isolated as described earlier.[46,47] PSII preparations were stored at −80 °C or 77 K (liquid N_2) until use. All work was conducted in the dark or under dim green light. For procedures used to form the S_0 state

see Supporting Information section S1.

2.2 EPR measurements. X-band (≈9 GHz) continuous wave (CW) EPR spectra were recorded at 4 K using a Bruker ELEXSYS E500 spectrometer equipped with an Oxford Instruments Ltd. ESR 900 liquid He-flow cryostat and an ITC503 temperature controller. Q-band (34 GHz) pulse EPR and ^{55}Mn-Davies ENDOR experiments were performed at 4.8 K on a Bruker ELEXSYS E580 spectrometer equipped with a homebuilt TE_{011} microwave cavity,[48] a CF935 liquid He cryostat, an ITC503 temperature controller (Oxford Instruments Ltd.) and an ENI 5100L radio frequency (RF) amplifier. W-band (≈94 GHz) measurements were performed at 5 K using a Bruker ELEXSYS E680 EPR spectrometer. All experiments were carried out employing a homebuilt ENDOR microwave cavity,[49,50] which comprised a solenoid of Teflon-coated silver wire integrated into a commercial W-band ENDOR probe head (Bruker). To ensure broadband microwave excitation and to minimize distortions, the loaded quality factor Q_L was lowered to 700 to obtain a microwave frequency bandwidth of 130 MHz. For further details on the EPR experiments, see Supporting Information section S2.

2.3 Spectral simulations. Spectra were fitted assuming an effective spin $S_T = 1/2$ ground state (see Supporting Information section S5.2). The basis set that describes the spin manifolds consisting of one electron and n interacting nuclear spins can be built from the product of the eigenstates of the interacting spins:

$$\left|\tfrac{1}{2}\, M\; I_1\, m_1 \ldots I_i\, m_i \ldots I_n\, m_n\right\rangle \qquad (1)$$

Here, M refers to the electronic magnetic sublevel, ±1/2; I takes the values 5/2 for ^{55}Mn and ^{17}O, and 1 for ^{14}N and ^{2}H; m_i takes the values $-I_i$, $1-I_i$, ..., I_i-1, I_i. The spin manifolds can be described by the following spin Hamiltonian:

$$\hat{H} = \beta_e \vec{B}_0 \cdot \hat{G} \cdot \vec{S} + \sum_i \left(-g_{n,i}\beta_n \vec{B}_0 \cdot \vec{I}_i + \vec{S} \cdot \hat{A}_i \cdot \vec{I}_i + \vec{I}_i \cdot \hat{Q}_i \cdot \vec{I}_i \right) \qquad (2)$$

It contains (i) the Zeeman term for the total electron spin, (ii) the hyperfine and (iii) nuclear Zeeman terms for either the metal ^{55}Mn or the ligand ^{14}N, ^{17}O or ^{2}H nuclei and (iv) the nuclear quadrupole interaction (NQI) term for the ^{14}N or ^{2}H nuclei (I = 1). The NQI splitting is not resolved in the EPR, ^{55}Mn-ENDOR and ^{17}O Electron-electron double resonance (ELDOR)-detected NMR (EDNMR) spectra.[51] Spectral simulations were performed numerically using MATLAB® (R2010a, The MathWorks, Natick, MA, USA), a vector-based linear algebra package, and the EasySpin toolbox.[52] For further information on data processing, details of the simulations and theory, see Supporting Information sections S3, S4 and S5, respectively.

2.4 Density functional theory (DFT) calculations. The computational models consist of 239–240 atoms and are obtained directly from the large set of possible S_0 state structures reported by Krewald *et al.*[40]. Additional calculations of hyperfine interaction (HFI) and NQI parameters were carried out using established methods,[20,28,29,53-60] on models with a spin doublet ground state based on the lowest energy broken-symmetry solution of each structure. These employed the TPSSh functional,[61] which is known to perform well for magnetic and spectroscopic properties.[54,62-65] All calculations were performed with ORCA[66] using the zeroth order regular approximation (ZORA)[67,68] for inclusion of scalar relativistic effects along with ZORA-TZVP (Mn, Ca, O, N) and ZORA-SVP (C, H) basis sets.[69,70] Tight SCF convergence criteria and integration settings were applied (Grid6 and IntAcc 6.0 in ORCA nomenclature), with more dense radial integration grids for Mn, N and O of 11, 9 and 9, respectively. The

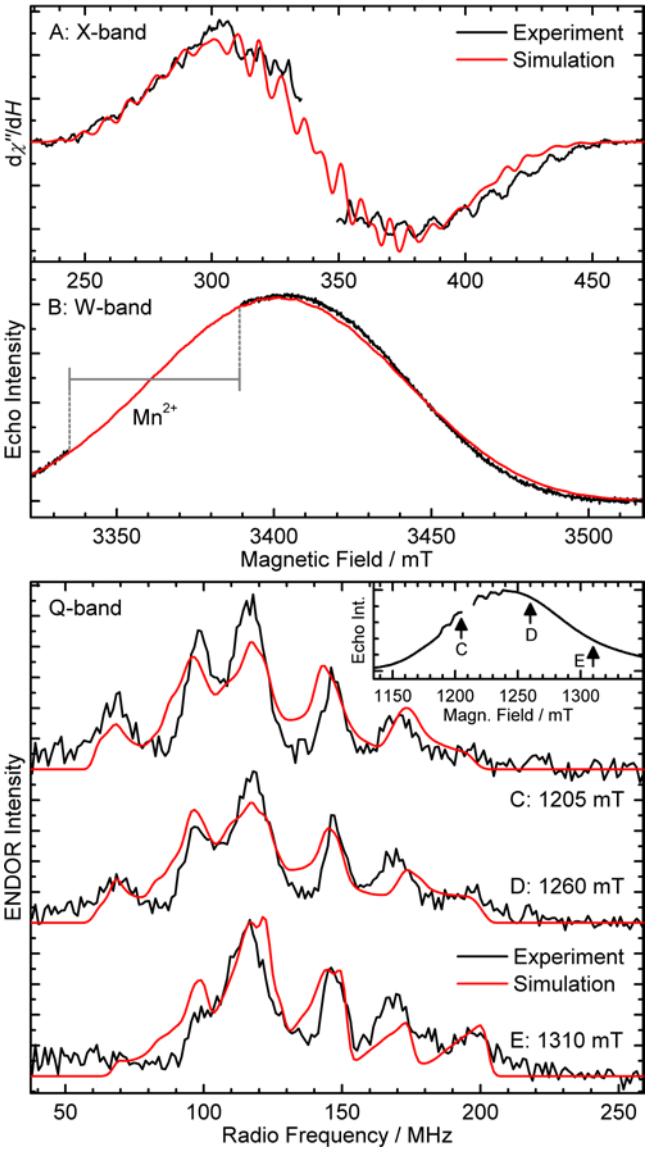

Figure 2. EPR and ^{55}Mn-ENDOR spectra (black traces) and spin Hamiltonian-based simulations (red traces) of PSII poised in the S_0 state. The optimized parameter set is given in **Table 1**. **Top: (A)** X-band CW EPR. **(B)** W-band electron spin echo (ESE)-detected EPR. Y_D had been replaced by a phenylalanine, removing the $Y_D^{\bullet}$ signal from the spectra.[45] **Bottom:** Q-band Davies ENDOR at **(C)** 1205 mT, **(D)** 1260 mT and **(E)** 1310 mT (see asterisks in the Q-band pulse EPR spectrum in the inset). The experimental Q-band ENDOR and EPR spectra represent the light-minus-dark differences. A decomposition of the simulation depicting the contribu-

tions from the individual ^{55}Mn nuclei is shown in Supporting Information **Fig. S2C**. In spectrum A and the inset, the $g \approx 2$ radical signal of $Y_D^{\bullet}$ (D2-Tyr160) was excised for clarity of presentation, as well as the region of contaminating Mn^{2+} in spectrum B. Experimental parameters: see Supporting Information Section S2.

calculations used the RIJCOSX approximation with GridX6,[71] and the decontracted basis sets of Weigend as auxiliary bases.[72] The electrostatic effect of the protein was simulated with a conductor-like screening model with a dielectric constant of 8.0.[73] The one-center approximation was applied and the spin-orbit coupling was evaluated with the effective potential/complete mean field approach. Picture change effects were taken into account in calculations of EPR properties.

3. RESULTS

3.1 EPR/ENDOR data of the S_0 state. In this study we performed all measurements on PSII isolated from thermophilic cyanobacteria, the same type of material used in current crystallographic studies.[21] Since all EPR/ENDOR data for the S_0 state had thus far been collected on PSII isolated from higher plants (spinach), a full EPR/^{55}Mn-ENDOR characterization was first performed prior to characterizing the exchangeable oxygen ligands of the Mn_4O_5Ca complex, to ensure the properties of the S_0 state complex are the same in both species.[34,74-80] These data (**Fig. 2**) constrain the electronic structure of the cofactor, mapping out the contribution of each Mn ion to the ground spin state. It can be readily observed that these data, particularly the Q-band ^{55}Mn-ENDOR, obtained in cyanobacteria are essentially the same as seen in earlier higher plant studies,[34] showing the cofactor in the S_0-state to be in an effective total spin $S_T = 1/2$ ground state. Importantly though, owing to the higher intrinsic activity of the cyanobacterial preparations normalized to total protein concentration, orientationally selective ENDOR data could be obtained, further constraining the ^{55}Mn HFI tensors (**Fig. 2C-E, Table 1**).

Table 1. Effective *G* and ^{55}Mn HFI Tensors A_i Used for the Simulations of the EPR and ENDOR Spectra of the Cyanobacterial S_0 (Fig. 3) and S_2 [29] States and the S_0 State in Spinach PSII[34].[a]

		G	A_i / MHz[b]			
			A_1	A_2	A_3	A_4
S_0	x	2.003	327	262	221	148
	y	1.965	314	217	188	164
	z	1.960	377	276	266	232
	iso[c]	1.976	339	252	225	181
S_0 [34]	x	2.009	320	270	190	170
	y	1.855	320	270	190	170
	z	1.974	400	200	280	240
	iso[c]	1.946	347	247	220	193
S_2 [29]	x	1.989	350	214	214	173
	y	1.978	329	195	184	157
	z	1.956	321	282	282	251
	iso[c]	1.974	333	230	227	194

[a] All *G* and A_i tensors are collinear. [b] The numbering of the A_i (i = 1–4) tensors is in descending order of the $A_{i,iso}$ values and does not correspond to the numbering of the Mn_i atoms. For an assignment of the A_i tensors to the Mn_i atoms, see Supporting Information Table S2. The isotropic components are the averages of the individual values: $G_{iso} = (G_x + G_y + G_z)/3$ and $A_{i,iso} = (A_{i,x} + A_{i,y} + A_{i,z})/3$.

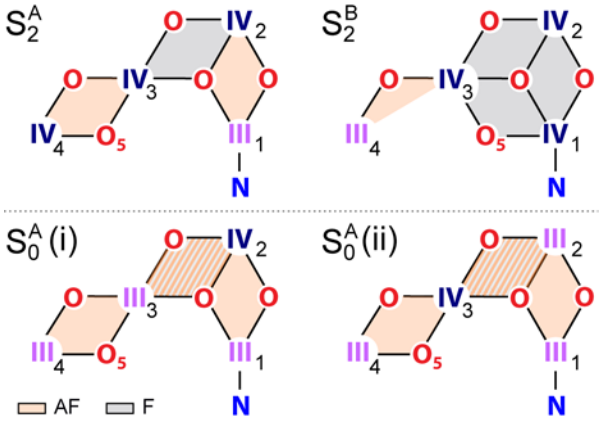

Figure 3. Exchange coupling topologies determined for the S_2[20,29,31,40,56] state and possible ones for the S_0 state (see **Fig. 9**) with three antiferromagnetic (AF) or ferromagnetic (F) interaction pathways (hatched areas: either AF or F interaction).

The ^{55}Mn HFI is derived from the coupling of the electron spin of the cofactor with the local nuclear spin of each Mn ion. The effective HFI parameters A_i provide a means to accurately describe the exchange coupling topology of the complex, which is to say, they allow an estimation of the magnitude of the magnetic interactions between the adjacent Mn ions of the complex (see Refs. [31,81]). The ^{55}Mn HFIs have been characterized in detail for the multiline EPR signal of the S_2 state.[34,79,82,83] Earlier work has shown that while these coupling parameters do not in principle correspond to a unique geometric structure, together with constraints derived from X-ray diffraction and EXAFS, it is best described in terms of a single structural motif, an open cubane-type structure.[20,29,31,40,55-57]

To rationalize the EPR/^{55}Mn-ENDOR data of this S_2 state form, the exchange coupling topology needs to fulfill two criteria: it must (i) render the complex low total spin ($S_T = 1/2$), and (ii) ensure all Mn ions contribute equally to the ground electronic state. This latter property is described in terms of spin projection coefficients, ρ_i, which in this instance are all approximately 1 (with only that of $Mn1$ being larger, **Table S1**). These two criteria are best explained by a set of three alternating net antiferromagnetic/ferromagnetic coupling interactions between $Mn1^{III}$, $Mn2^{IV}$, $Mn3^{IV}$ and $Mn4^{IV}$ (S_2^A in **Fig. 3**).[20,29,31,40,56] As the same spin state and similar HFI parameters (**Table 1**) are observed for the S_0 state, a similar coupling topology of predominately antiferromagnetic coupling interactions is therefore expected. There remains though an ambiguity

as to the precise individual oxidation states of the four Mn ions.

3.2 The Mn1-His332-imino-N interaction: a local probe for the electronic structure. In addition to ^{55}Mn HFIs, the HFI and NQI of first coordination sphere ligands provides a means to assess the electronic structure of the cofactor (see Ref. [81]). Ligand HFIs have the advantage that they provide site information, namely the local oxidation states of the Mn ion to which they are bound. The imino-N of His332 ligated to Mn1[1,2] is one such example. In the low-spin S_2 state, the large HFI associated with the imino-N[28,29,84-88] requires Mn1 to carry the largest spin projection coefficient. This means it must represent the Mn of lowest oxidation state, and thus it can be assigned to the +III oxidation level[28,29,87,88] as in the S_2 state, the cofactor contains only Mn ions poised at +III or +IV level.[20,29,31,40,57] A similar approach can be used to characterize the oxidation level of Mn1 in the S_0 state.

Q-band ^{14}N three-pulse electron spin echo envelope modulation (ESEEM, **Figs. 4, Figs. S3-S5**) and ^{14}N hyperfine sublevel correlation (HYSCORE, **Fig. 5**) were used to characterize the imino-N His322 ligand in the S_0 state. **Fig. 4** shows ESEEM spectra for the S_0 state, compared with the S_2 [29] state. The Fourier-transformed ESEEM spectra from both S states are very similar, containing the same three features: a set of lines centered at frequencies below 2.5 MHz ($\nu_\beta = \nu_n - |A_{iso}|/2$), single-quantum transitions between ≈5 and ≈9 MHz ($\nu_\alpha = \nu_n + |A_{iso}|/2$) and less

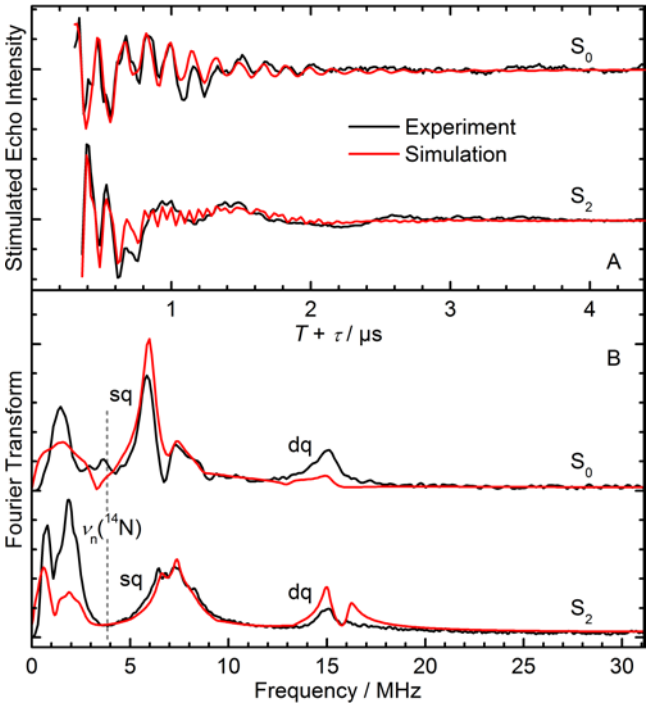

Figure 4. Q-band three-pulse ^{14}N-ESEEM light-minus-dark spectra of the imino-N His322 ligand in PSII poised in the S_0 state. For comparison, the S_2 state signal is also shown, see Ref. [29]. **A:** time-domain traces; **B:** corresponding Fourier transforms. Black lines represent baseline-corrected experimental spectra, red lines spin Hamiltonian-based simulations. Fit parameters are listed in **Table 2**. "sq" and "dq" refer to the position of single and double-quantum transitions, respectively. The full set of field- and τ-dependent three-pulse ESEEM spectra are shown in **Figs. S3-S5**. Experimental parameters: microwave frequencies: 33.965 GHz (S_0), 34.037 GHz (S_2); magnetic fields: 1245 mT (S_0), 1250 mT (S_2); shot repetition times: 0.5 ms (S_0), 1 ms (S_2); microwave pulse lengths ($\pi/2$): 16 ns (S_0), 12 ns (S_2); τ: 260 ns; ΔT: 48 ns (S_0), 100 ns (S_2); temperatures: 4.8 K (S_0), 5.2 K (S_2).

Table 2. Fitted ^{14}N HFI and NQI Tensors in MHz for the His332 Imino-N in the S_0 and S_2[29] States, and Computed Values for the DFT Models S_0-A, S_0-B, S_0-C (Section 3.5).

	Exp.[a]		DFT		
	S_2 [29]	S_0	**S_0-A**	**S_0-B**	**S_0-C**
$\lvert A_{iso}\rvert$ [b]	7.1	5.3	5.5	4.2	3.3
A_{dip} [c]	0.75	1.03	0.52	0.53	0.32
A_η [d]	0.81	0.97	0.29	0.24	0.51
$\lvert e^2Qq/h\rvert$	1.97	1.78	1.90	2.00	1.98
η [d]	0.75	0.75	0.71	0.62	0.65

[a] The G tensors used were those fitted to the corresponding EPR/^{55}Mn ENDOR spectra (**Table 2**). The Euler rotation angles [α, β, γ] of the NQI relative to the A tensors are [23, 111, 15] in the S_0 and [20, 12, 0] for the S_2[29] state simulations. [b] A_{iso} is defined as the average of the principal components of the HFI tensor (**Table S3**). [c] A_{dip} is defined in terms of T_1, T_2, and T_3 as $A_{dip} = (T_1 + T_2)/2 = -T_3/2$. T_1, T_2, and T_3 represent the three principal components of the HFI tensors minus A_{iso} and of the NQI tensors and are labeled such that $|T_1| \le |T_2| \le |T_3|$. [d] The rhombicity is defined by A_η or $\eta = (T_1 - T_2)/T_3$, respectively.

intense double-quantum resonances around 15 MHz ($\nu_{2\alpha} = 2\nu_n + |A_{iso}|$). This requires the ^{14}N His332 hyperfine and quadrupole interactions to be approximately the same in both the S_2 and S_0 state. Corresponding Q-band HYSCORE data allow the ^{14}N HFI and NQI parameters to be further constrained. In the 2D-HYSCORE surface, the three features that the Q-band ESEEM spectra comprise appear as cross peaks in the (+,+) quadrant (**Fig. 5**), which spread inwards towards the diagonal as opposed to extending parallel to the frequency axis. Both these features are consistent with the ^{14}N HFI being slightly smaller in S_0 than in the S_2 state, i.e. the HFI is further away from the "cancellation condition" (see Ref. [29]).

Fitted spin Hamiltonian parameters for collective simulation of the ESEEM and HYSCORE data are listed in **Table 2**. The magnitude of the isotropic HFI A_{iso} and the NQI ($|e^2Qq/h|$) are slightly smaller than in the S_2 state, while the anisotropic (dipolar) HFI component A_{dip} is slightly larger as compared to the values seen for the S_2 state. Nevertheless, the strong similarity of the hyperfine and quadrupole interactions in both the S_0 and S_2 states, and comparison to ^{14}N ligands in model complexes[89-94] assign Mn1 the same oxidation state (+III) and ligand field (5-coordinate square pyramidal) in both the S_0 and S_2 states (Supporting Information section S9.2).

Importantly, the large A_{iso} value demonstrates clearly

that the Mn1 ion must carry the largest spin projection factor of the complex,[89-93] similar to the situation in the S_2 state. This means that Mn1 must represent a manganese ion of lowest (or equal lowest) oxidation state of the Mn ions in the cluster, confirming that no Mn^{II} ion, which would then exhibit the largest spin projection factor, can be present in the S_0 state. With the oxidation state pattern III,III,III,IV it remains unclear where the Mn^{IV}

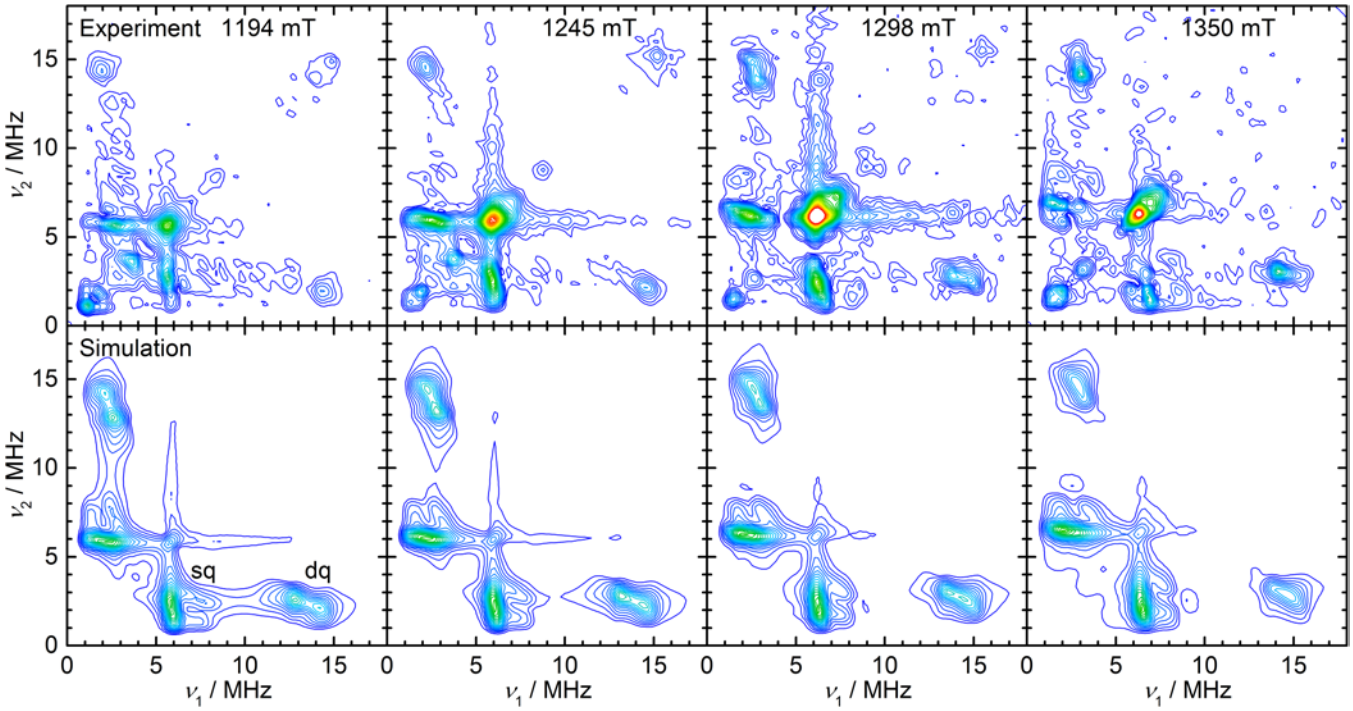

Figure 5. (+,+) quadrants (ν_1, ν_2 > 0 MHz) of the Fourier-transformed Q-band ^{14}N-HYSCORE experimental spectra **(top)** and spin Hamiltonian-based simulations **(bottom)** of PSII in the S_0 state. The varying magnetic-field positions correspond to g = 1.798–2.032. "sq" and "dq" point out regions of single- and double-quantum transitions, respectively. The optimized simulation parameters are listed in **Table 2**. Experimental parameters: microwave frequencies: 33.966 GHz (1194 mT, 1245 mT), 33.964 GHz (1298 mT, 1350 mT); magnetic fields: 1194–1350 mT; shot repetition time: 0.5 ms; microwave pulse length ($\pi/2$): 16 ns; τ: 260 ns; ΔT: 96 ns; temperature: 4.8 K.

position is. Chemical modeling suggests Mn1 and Mn4 have similar redox potentials,[20] as either site can stabilize the only Mn^{III} in the S_2 state. Thus, the most likely candidate for the Mn^{IV} site in S_0 is either Mn2 or Mn3 (**Fig. 3**).

3.3 Exchangeable oxygen ligands of the Mn tetramer. As recently demonstrated in our laboratory,[27-29,51] W-band EDNMR is the method of choice to characterize interactions of ^{17}O with the Mn tetramer of the OEC. **Fig. 6** shows ^{17}O-EDNMR spectra of the single-quantum region for the S_0 and the S_2 state[29] after $H_2{}^{17}O$ buffer exchange in the S_1 (dark) state. It can be immediately observed that the ^{17}O spectral profile of the S_0 state, not present in non-enriched buffer (**Fig. S6**), is similar in appearance to that of the S_2 state,[27-29] albeit slightly broader and somewhat better resolved. Additional ^{17}O resonances can be observed in the double-quantum region (**Fig. S6**).

A full spin Hamiltonian-based analysis of ^{17}O-EDNMR data was not performed as spectra could only be collected and simulated (**Fig. 6**, **Table S4**) at the EPR signal maximum due to the fast magnetic relaxation properties of the S_0 state (faster than the S_2 state). Nevertheless, as also seen for the S_2 state,[27] three ^{17}O HFIs are required to reproduce the entire ^{17}O signal envelope including the double-quantum region (**Fig. S6**): (i) a large coupling of ≈10 MHz, (ii) an intermediate coupling of ≈4 MHz and (iii) matrix couplings of <1 MHz. Likewise, we assign these three couplings to (i) an exchangeable oxygen bridge, (ii) (a) terminal oxygen ligand(s) and (iii) matrix water including water bound to the Ca^{2+} ion. Since for both the S_0 and the low-spin S_2 state spectra, ^{17}O exchange occurred in the S_1 state, their large similarity consequently implies that the labelled oxygen bridge position is identical in the two states, i.e. O5 (see Discussion). The protonation state of the exchangeable oxygen bridge is less clear, i.e. μ-oxo or μ-hydroxo. We do however stress that this signal is not consistent with a bridging water ligand. In the model system Mn catalase, terminal water bound along the JT axis of Mn^{III} displays only a small ^{17}O HFI (<1 MHz).[95]

3.4 A protonated μ-OH bridge species. If any of the oxygen bridges in the complex represents a μ-hydroxo, the proton of the bridge should exhibit a comparatively strong electron-nuclear HFI. To observe such species, PSII samples can be resuspended in ^2H_2O buffer to isolate all exchangeable, solvent-accessible protons, i.e. potential substrate sites. ^{2}H interactions in the S_0 state were examined in PSII from higher plants at low frequency (X-band ESEEM), with modeling suggesting a large coupling, which could be consistent with a μ-hydroxo bridge.[96-98] In previous experiments on Mn/Fe metallocofactors,[99] we

have been best able to resolve large ^{2}H interactions by Q-band ESEEM/HYSCORE spectroscopy, which partially suppresses matrix water contributions. We note that in addition to protons of potential substrates, all O- and N-bound ^{1}H are expected to quantitatively exchange during the incubation time used (2 hours). For the S_2 state, the ^{1}H and ^{2}H hyperfine splittings seen in Davies and Mims ENDOR, respectively, were shown to be too small to originate from a hydroxo bridge.[27]

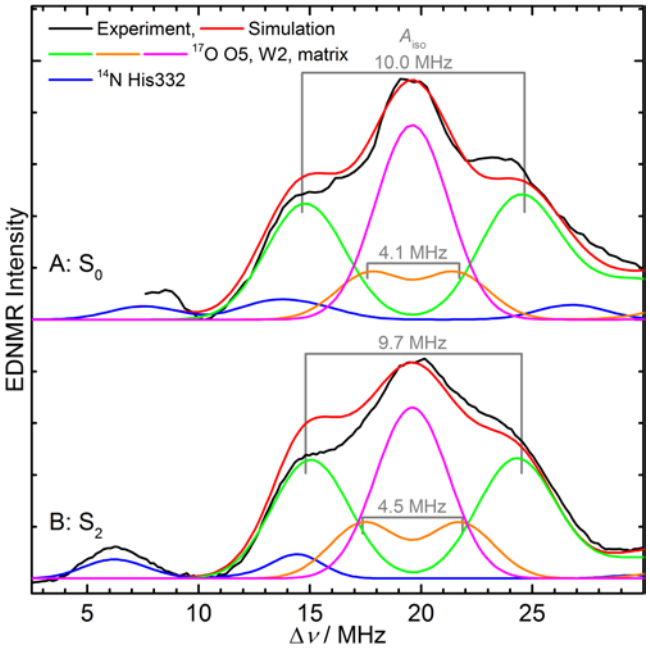

Figure 6. W-band EDNMR spectra of $H_2{}^{17}O$-exchanged PSII samples in the S_0 **(A)** and in the S_2[29] **(B)** state. Black traces depict the single-quantum region of background-corrected experimental spectra; superimposed red traces represent spin Hamiltonian-based simulations. Colored lines represent a decomposition of the simulations showing contributions from the individual ^{14}N and ^{17}O nuclei. The optimized parameter sets are listed in **Table S4**. For experimental parameters and double-quantum regions, see **Fig. S6**.

Three-pulse ESEEM data of S_0 state PSII samples after $^{2}H_2O$ buffer exchange are shown in **Fig. 7**. Note that the data represent a ratio of raw ESEEM traces collected on samples in ^{2}H-labeled and non-labeled (no ^{2}H signal) buffer to suppress the background ^{14}N His332 signal. The relevant spectra are collected on the high-field edge of the S_0 multiline spectrum. This is because all samples contain a small $[Mn(H_2O)_6]^{2+}$ contamination, which, owing to its slower magnetic relaxation, can strongly perturb our S_0 data, as demonstrated in the Supporting Information: In **Fig. S7**, three-pulse ESEEM spectra measured at two field positions within the S_0 multiline signal envelope are shown. The lower field position (1194 mT, g = 2.035) overlaps with the intense component of the hexaquo-Mn^{2+} signal whereas at the higher field position (1326 mT, g = 1.832), the same as used in **Fig. 7**, the Mn^{2+} signal is outside this region. Under conditions optimized to best visualize the S_0 multiline (S_T = 1/2, $\pi/2$ = 12 ns), the Fourier transforms of ESEEM spectra collected at both these field positions superimpose sharp ^{2}H and broader ^{14}N (His332) signals centered around their respective Larmor frequencies. Importantly though, at the lower field, the ^{2}H peak is twice as intense, suggesting it is representative of both ^{2}H ions of the S_0 state and of the background Mn^{2+} complex. This can be shown by repeating the same experiment now under conditions optimized to best visualize the hexaquo-Mn^{2+} signal (S = 5/2, $\pi/2$ = 8 ns). The corresponding Fourier transforms resolve now only a sharp ^{2}H signal at the low field position, representative of the water ligands of the Mn^{2+} complex, with no corresponding peak at the

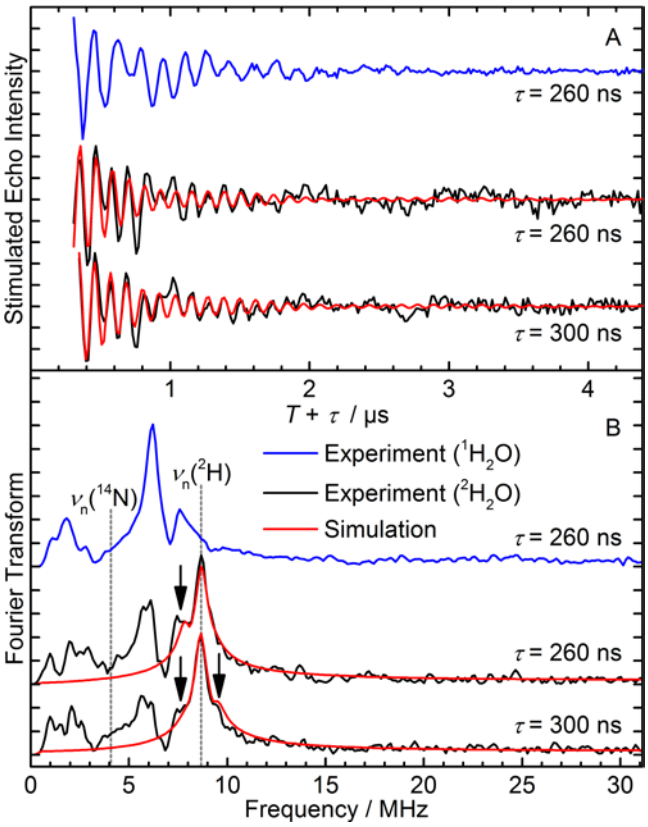

Figure 7. Q-band three-pulse ^{2}H-ESEEM of PSII in the S_0 state, measured in the high field region (g = 1.832) of the corresponding Q-band multiline EPR spectrum. **(A)** time-domain traces; **(B)** corresponding Fourier transforms. Black lines represent baseline-corrected experimental data after taking the time-domain ratio of traces from $^{2}H_2O$- and non-exchanged (blue lines) samples. Red lines represent spin Hamiltonian-based simulations, which includes strongly and weakly coupled ^{2}H nuclei at ratios 1:3 (1326 mT). Black arrows indicate features due to a large, τ-dependent, non-matrix ^{2}H coupling. Experimental parameters: microwave frequency: 34.008 GHz; magnetic field: 1326 mT; shot repetition time: 0.5 ms; microwave pulse length ($\pi/2$): 12 ns; τ: 260, 300 ns; ΔT: 48 ns; temperature: 4.8 K.

high field position. Hence, ESEEM measurements at the high field position can be considered free of any Mn^{2+} contribution.

Fourier transforms of the three-pulse ESEEM data, from which the ^{14}N signal from the His332 has been removed by taking the ratio of ^{2}H-labeled and non-labeled spectra in the time domain, are shown in **Fig. 7B**. Closer inspection of these spectra reveals that in addition to the ^{2}H 'matrix'

peak centered at the ^{2}H Larmor frequency, there is a second spectral feature in the form of shoulders whose appearance is dependent on the τ value used (black arrows). This behaviour can be reproduced by spin Hamiltonian-based simulations using a HFI tensor A = [1.91 0.35 0.57] MHz and NQI of $|e^2Qq/h|$ = 0.27 MHz, η = 0.61 (see also **Figs. S8, S9, Table S5**). This indicates that this feature comes from a more strongly coupled ^{2}H nucleus ($A_{\|}(^2H)$ = 1.91 MHz ≙ $A_{\|}(^1H)$ = 12.4 MHz). The simulation included the matrix component which was parameterized using values typical of water/hydroxo Mn terminal

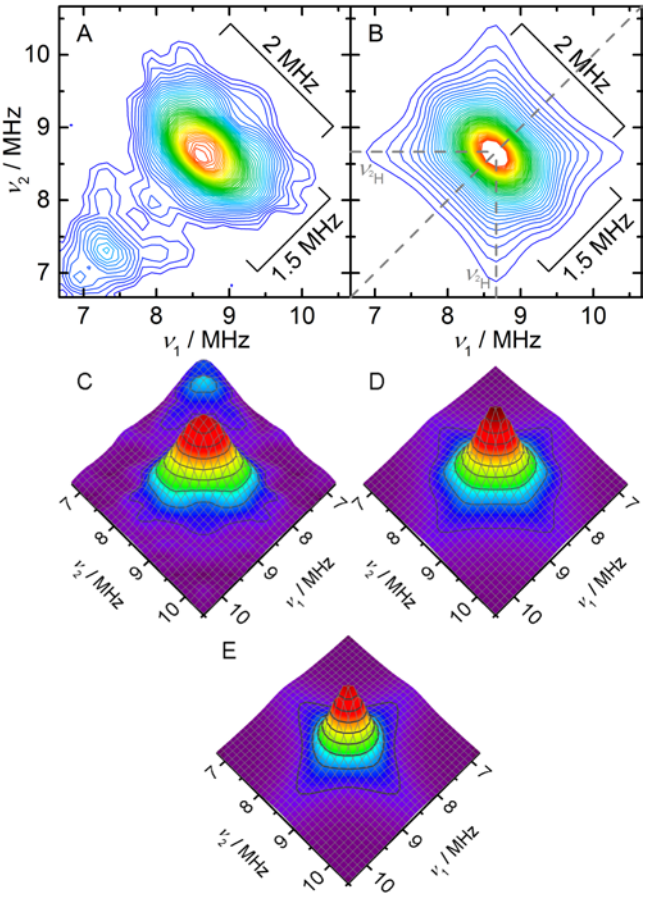

Figure 8. Section of the (+,+) quadrant of **(A), (C)** the Fourier-transformed Q-band ^{2}H-HYSCORE spectrum of a ^2H_2O-exchanged PSII sample in the S_0 state, measured at the high-field edge (g = 1.832) of the corresponding Q-band multiline EPR spectrum and **(B), (D)** a simulation thereof (1:3 ratio of strongly and weakly coupled ^{2}H nuclei), once **(A), (B)** as contour plots and once **(C), (D)** as 3D surfaces. Panel **(E)** shows a 3D surface of the simulation of only the three weakly coupled nuclei (see **Fig. S10B, C**) The full frequency space of the (+,+) quadrant is depicted in **Fig. S10A**. Experimental parameters: see **Fig. S10**.

ligands (i.e. hexaquo-Mn^{2+}-like,[51] **Table S5**). The ratio of the two species was 1:3 (strongly coupled to terminal ligands, i.e. W1/W2) at the high field position and, due to the additional hexaquo-Mn^{2+}, 1:6 at the low field position (**Fig. S8**).

To confirm that there was a second, strongly coupled ^{2}H species present in our ESEEM data, 2D HYSCORE measurements (**Figs. 8A, S10A**) were performed at the high-field edge of the S_0 multiline spectrum. These data reveal an intense ^{2}H cross peak centered at the ^{2}H Larmor frequency (ν_n = 8.67 MHz) of width (≈1 MHz) consistent with terminal water ligands. Zooming in, a second structure is seen underneath this strong feature, a broadened cross peak of structure consistent with simulations of the three-pulse ESEEM data. The cross peak is both broadened along the diagonal and at 90° to the diagonal suggesting that this ^{2}H nucleus displays a substantial NQI, consistent with the simulations, shown in **Fig. 8B**.

The larger HFI and NQI of this species support assigning it to a μ-hydroxo bridging ligand. $|e^2Qq/h|$ = 0.27 MHz inferred from simulation is on the higher end, yet within the limits from the empirical model of Soda and Chiba[100,101] for asymmetrically hydrogen-bonded deuterons (0.31 MHz). In the earlier X-band ESEEM experiments, the time-domain traces were simulated employing larger dipolar (and smaller isotropic) HFI constants ($|A_{dip}|$ ≈ 0.8-0.9 MHz, A_{iso} ≈ 0.3-0.4 MHz)[96-98] than in our simulations ($|A_{dip}|$ ≈ 0.48 MHz, A_{iso} ≈ 0.94 MHz), however, ignoring ^{2}H NQI terms. Our Q-band ESEEM/HYSCORE data show that a comparatively large NQI is instead crucial to correctly reproduce the line shape and width. We note that the hyperfine splitting, while being distinctly larger than that of the terminal water ligands, is at least two times smaller than that seen for μ-hydroxo ligands in similar, dimeric systems. The larger HFI in these simpler exchange-coupled systems comes about because one of the metal ions carries a large spin projection (ρ ≈ 2).[99] As outlined in section 3.2, Mn1, the Mn that ligates His332, carries the largest spin projection, and as such, a protonated bridge that involves Mn1 should have a spectral signature most like the simpler model systems. As the experimental value is lower, it is likely that the protonated bridge does not involve Mn1, but instead is located at the other end of the complex, i.e., it is ligated to Mn3 and/or Mn4 which carry spin projections ρ ≈ 1. This would then assign either O4 or O5 as the location of the μ-hydroxo bridge.

3.5 DFT models for the S_0 state. The EPR and double resonance measurements described above require the S_0 state to have (i) an electronic ground-state spin of S_T = 1/2, (ii) the oxidation states $Mn^{III}_3Mn^{IV}$, (iii) a Mn^{III} ion in an approximately 5-coordinate square-pyramidal ligand field in the Mn1 position, as in the low-spin S_2 state, and (iv) a protonated oxo bridge, which could be O4 or O5. The S_2 state contains two interconvertible structures,[20] in which all μ-oxo bridges are unprotonated, with H_2O in the W1 position and OH^- in the W2 position (**Fig. 1C**, **Fig. 9**).[56] In the S_1-S_2 transition, one electron is lost, whereas in the S_0-S_1 transition, one electron and one proton are lost from the catalytic center.[32,33] Thus, an S_0 state model that could lead to the interconvertible S_2 forms must have one additional proton and two more electrons. There are then three possible protonation sites: the μ-oxo bridges O4 and O5 and the terminal OH^- ligand W2, all of which were examined recently.[40] Only three models were found that exhibit the correct S_T = 1/2 ground state at the protonation level that corresponds to the spectroscopically consistent S_2 state models: **S_0-A**, **S_0-B** and **S_0-C**, (**Fig. 9**). **S_0-A**

and **S₀-B** have the same protonation pattern as a model proposed by Siegbahn[35,36] (protonated O5, W1 = H_2O, W2 = OH^-), while the protonation pattern of **S₀-C** resembles that proposed by Saito *et al.*[41] in a QM/MM study of the deprotonation pathways during the S_0-S_1 transition. We note that computational models for the S_0 state with a different total number of protons have also been proposed in the literature.[37-39] These are not explicitly treated here but have been evaluated previously.[40] Only one model with an additional proton compared to models **S₀-A**, **S₀-B** and **S₀-C** was predicted to have a ground state of

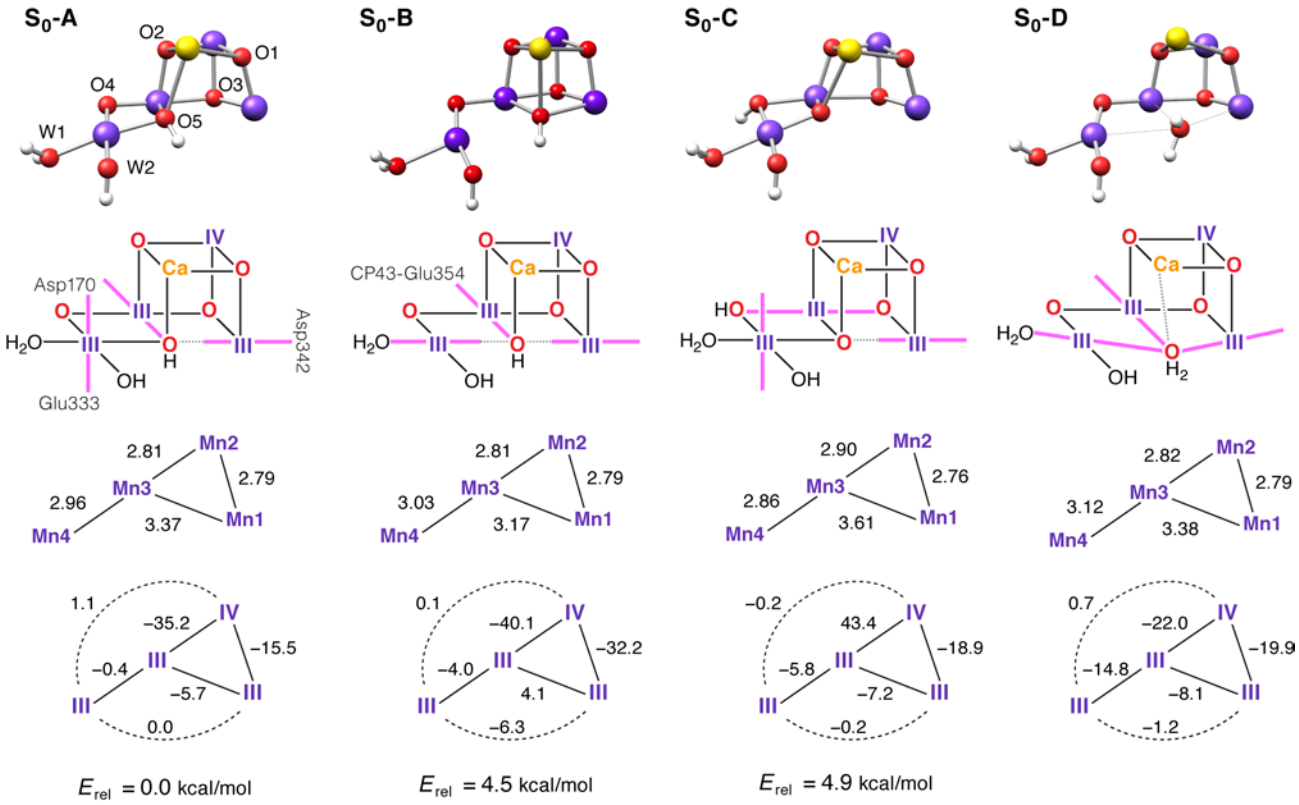

Figure 9. Top: 3D and schematic representations of DFT models for the S_0 state. Orientations of JT axes are indicated by magenta bars. **Middle:** Mn-Mn distances in Å. **Bottom:** Mn oxidation state distributions and exchange coupling constants in cm^{-1} (using the $-2J$ convention for the Heisenberg-Dirac-van Vleck Hamiltonian). All models have a spin $S_T = 1/2$ ground state and an $S_T = 3/2$ first excited state. Relative energies are given for the three isomeric forms that carry the same number of protons.

$S_T = 1/2$, albeit it was among the least energetically favorable in that set of isomers. This is model **S₀-D**, in which O5 is a water ligand. Note that in this circumstance, O5 cannot represent the large ^{17}O HFI of the exchangeable bridge, which would instead be assigned to another oxygen bridge, e.g. O4.

Fig. 9 shows 3D depictions of the $Mn_4CaO_5W_2$ cores, followed by schemes showing the JT axis orientations, then Mn–Mn distances and finally the computed exchange coupling constants. The four models share the same oxidation state distribution with Mn2 representing the Mn^{IV} ion. **S₀-A** and **S₀-B** have the same protonation pattern, but they differ in the direction of the Mn4 JT axis: it is oriented approximately perpendicular to the plane spanned by Mn3, O4 and Mn4 in **S₀-A,** while it lies along the W1-Mn4-O5 vector in **S₀-B**. It is not strictly correct to describe **S₀-A** and **S₀-B** as open/closed cubane isomers in analogy to the S_2 state since the Mn1 JT axis leads to long Mn1-O5 distances (>3 Å) in both structures. In **S₀-C**, O4 is protonated and the Mn3 JT axis is oriented along O3-Mn3-O4, leading to a different exchange coupling topology (ferromagnetic coupling between Mn2 and Mn3 as opposed to antiferromagnetic coupling in **S₀-A** and **S₀-B**). In **S₀-D**, all JT axes point towards the doubly protonated O5, similar to model **S₀-B**. The isomers **S₀-A**, **S₀-B** and **S₀-C** are relatively close in energy, with **S₀-A** being energetically favored (no energetic comparison can be made with **S₀-D** as it is not an isomer).

Overall, all models, irrespective of their protonation state, contain three short (2.74–2.96 Å) Mn-Mn distances, and one longer Mn-Mn distance of >3.3 Å, consistent with EXAFS constraints.[42,43] While all four models are structurally similar, their magnetic properties differ.[40] The ^{55}Mn HFIs for **S₀-A, S₀-B** and **S₀-C** are all similar and consistent with experimental data. In contrast, **S₀-D** exhibits too small ^{55}Mn couplings, well outside experimental bounds (up to ≈90 MHz), excluding that O5 is doubly protonated, i.e. a water molecule. The His332 ^{14}N HFI differs among the remaining subset of structures (**Table 2**). While the DFT calculations systematically underestimate the experimental A_{dip} and A_η values, which represent the pronounced HFI tensor anisotropy, the isotropic coupling strength serves as a sensitive probe for the electronic structure of the models. **S₀-A** exhibits the largest A_{iso},

close to experiment (and to 5.8 MHz as calculated for the low-spin S_2 state)[29], but **S_0-B** also shows reasonable agreement. The value calculated for **S_0-C** however is too small, owing to the small spin projection on Mn1 (**Table S2**) arising from its different exchange-coupling topology. Also the experimental NQI parameters are best matched by those computed for **S_0-A**. To summarize, the calculations presented here favor an S_0 structure which contains a singly protonated O5, and disfavor a doubly protonated O5 or a singly protonated O4.

4. DISCUSSION

The EPR results described above constrain the structure and protonation state of S_0. As expected, its geometric structure is similar to the low-spin S_2 state, but with the O5 present as a μ-hydroxo bridge. The structure however is more complicated in that it contains three Mn^{III} ions, leading to a number of energetically close Jahn-Teller isomers. This may explain the strong species dependence of S_0 state EPR signals and their sensitivity to small molecules,[78,102] which suggests that the cofactor can access multiple magnetic states. Nevertheless, while structural details remain ambiguous, we present clear experimental evidence that the cofactor contains an exchangeable oxygen bridge, which appears to be protonated. In the following, while we cannot definitively rule out O4 as the hydroxo bridge, we rationalize the assignment of the exchangeable oxygen bridge to O5, the same as in the S_2 state, and, as a consequence, as one of the substrates of the water splitting reaction.

4.1 Assigning O5 as the exchangeable oxygen bridge. In the S_2 state, the large ^{17}O HFI was assigned to a single exchangeable oxygen (oxo) bridge, the O5 bridge.[27-29] This result was based on site perturbation(s) of the cofactor – it was seen that changing the immediate environment around the O5 bridge altered the ^{17}O HFI. In our experiments on both the S_2 and S_0 states, $^{16}O/^{17}O$ exchange takes place during incubation in $H_2{}^{17}O$ buffer in the S_1 state prior to flash-induced S-state advancement. Thus, oxygen sites exchangeable in S_1, such as O5, should be ^{17}O-labeled both in S_2 and S_0 state experiments. This is also the case if the exchangeable site represents a substrate, which has then been replenished upon O_2 release by a water molecule from its surrounding. Hence, the large ^{17}O HFI of a labeled oxygen bridge observed in the S_0 state can be assigned to O5.

4.2 O5 as the μ-hydroxo bridge. The question that then needs to be asked is: if O5 is an exchangeable hydroxo bridge as opposed to an oxo bridge, would we expect its HFI to remain approximately the same? We have partially addressed this question recently in a study of HFI constants of bridging ligands in model systems.[95] Model complexes and computational modeling predict that the HFI of an oxygen bridge in exchange-coupled Mn dimers should increase upon protonation. While this is counterintuitive considering that protonation should lead to a lowered covalency of the Mn–μO bond, the larger HFI can be rationalized by an increase of s-orbital character found for the Mn–μO bond and thus of spin-core polarization. In silico, the coupling is expected to increase by a factor of two for simple dimer systems assuming no change occurs in the oxidation states of both Mn ions. Clearly, here we do not see such a large change; the maximum would be a ≈10% increase as compared to S_2 state data. We suspect that the oxidation state change of the two Mn ions that ligate this oxygen (i.e. Mn4 and Mn3), resulting in a lowering of covalency of the Mn–μO bonds, could possibly act to outbalance the effect of bridge protonation.

4.3 Assigning O5 as the slowly exchanging substrate W_s in the S_0 and S_2 states. The ^{17}O signals observable in the S_0 state originate either from oxygen species exchangeable in S_1 or from a substrate newly bound after O_2 formation and release. The fact that no additional ^{17}O interactions are observed in S_0 as compared to S_2, thus limits the possible candidates for W_s to those ^{17}O species that have been identified in S_2 and thus precludes any oxygen bridges other than O5 from representing W_s.

Mass spectrometry measurements have shown that the two substrate waters bound to the cofactor exchange at different rates with bulk water,[13,14] demonstrating the two sites are not chemically equivalent. One substrate, termed the slowly exchanging water (W_s) exchanges on a seconds timescale, while the second substrate, termed the fast exchanging water (W_f) exchanges on a sub-second timescale. Rates for W_s have been measured in all S states, with rate constants of S_0: ≈10 s^{-}, S_1: ≈0.02 s^{-1}, S_2: ≈2 s^{-1} in spinach thylakoid membranes at 10 °C.[13,14] This requires that W_s is bound in all S states, including S_0. The general trend is a slowing of the rate with the increasing net oxidation state of the cofactor. This is as expected because it is the acidity of bound oxygen that governs its exchangeability; if there is a high barrier to protonation of the oxygen ligand, the site is non-exchangeable.[103,104] As the oxidation state of Mn changes from +III, to +IV, the acidity of a bridging oxygen ligand will increase dramatically (9-10 pK_a units in $[Mn_2(\mu\text{-}O)_2(bpy)_4]^{n+}$).[104] The protonation of the exchangeable oxygen to yield a bound water molecule prior to exchange with a solvent water molecule is therefore energetically more costly in a Mn^{IV} compared with a Mn^{III} ion, slowing the exchange rate. It is clear from the DFT calculations that the acidity of O5 is lower in the S_0 state as compared to S_2, with calculations favoring O5 being protonated as opposed to O4 or any other oxo bridge. Only the O5 bridge, but none of the exchangeable terminal water ligands W1-W4, changes its protonation state going from S_0 to S_1/S_2 and thus assigning O5 as W_s, the exchange rate of which decreases, readily explains the results presented here.

In addition, absolute rates of exchange favor assigning O5 to W_s. In model systems, terminal water ligands (H_2O/OH) of Mn in the +III and +IV oxidation state and Ca all exchange with rates on a micro- to nanosecond timescale, much faster than that observed for W_s, but rather consistent with W_f.

Historically, bridging oxygen ligands, which must represent oxo ligands in the higher S states (S_2, S_3), have been less favored as substrates of the reaction because these ligands exchange very slowly in model systems.[103-105] This,

however, is clearly not the case of the unique O5 bridge, which by virtue of its flexible coordination (**Figs. 2C, 10**)[20,31] has more degrees of freedom and thus displays an enhanced exchange rate as compared to simpler models. Whether this flexibility simply overcomes steric constraints of water access to the O5 bridge or tunes bridge acidity to energetically lower substrate exchange transition states, we cannot say for certain. Although, as O_4 is also accessible by solvent via a water channel terminating at Mn4,[1,21] we favor an effect on bridge acidity at least partly contributing to the enhanced exchange rate.

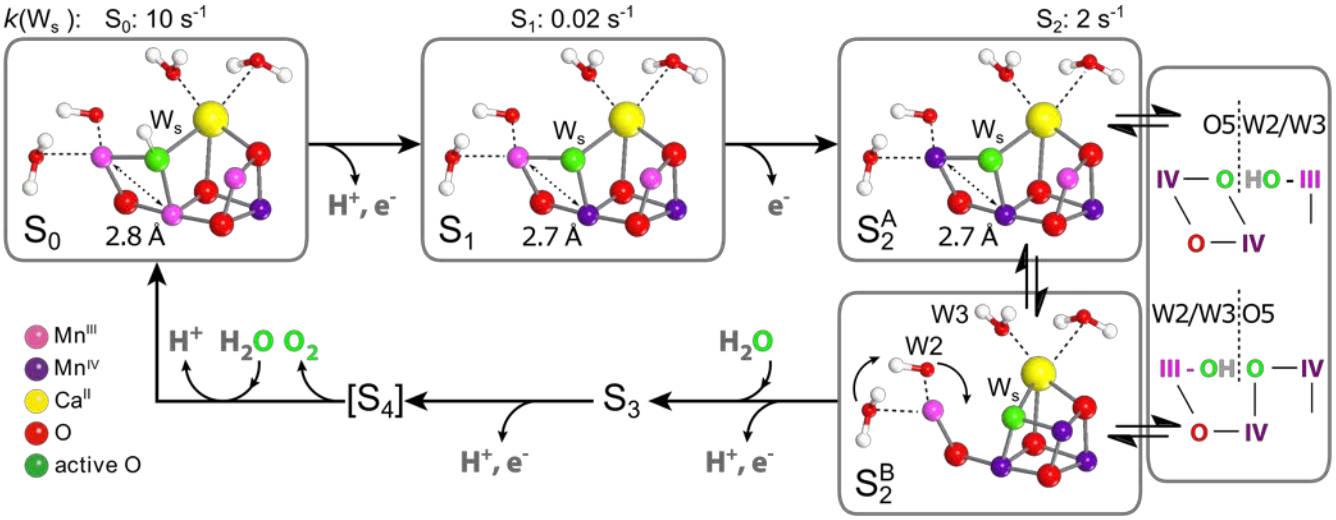

Figure 10. Mn_4O_5Ca cluster models including directly bound H_2O/OH^- ligands in the states S_0, S_1 and S_2 of the reaction cycle, visualizing Mn oxidation state changes, substrate binding, deprotonation and oxygen release events, also considering the results presented in this work. Furthermore, Mn3-Mn4 EXAFS distances[42,43], as well as exchange rates *k* of W_s[13,14], consistent with the assignment of W_s to O5, are shown for the individual states.

Our basis for invoking the structural flexibility of W_s/O5 as key to understanding its exchange rate is based on the observation that, while the rate of W_s exchange slows upon oxidation of the cofactor, it is slower in the S_1 state as compared to the S_2 state. The flexible coordination of O5 may not be critical in the S_0 state as it represents a hydroxo ligand. A protonated bridge, unlike a fully deprotonated bridge, should be fast exchanging compared with model systems.[103,104] However, a similar mechanism as assumed for the equilibrium between S_2^A and S_2^B (**Fig. 10**, left), involving proton transfer between a terminal H_2O/OH^- ligand and O5, could be in effect in the S_0 state for the interchange between the two protonation isomers **S_0-A** and **S_0-B**, which differ in energy by 4.5 kcal/mol. It is however noted again that the spin-coupling topology of **S_0-B** leads to Mn spin projection factors (**Table S2**) that result in larger deviations from experimental ^{55}Mn and His332 ^{14}N hyperfine couplings (**Table 2**) than that of **S_0-A**. Upon deprotonation to form the S_1 state, the exchange rate of O5 dramatically slows down. While the cofactor does not display redox isomerism in the S_1 state, recent experiments indicate the existence of two different S_1 state forms,[106] which could differ with regards to the JT axes of the two Mn^{III} ions (compare S_0 state models **S_0-A** and **S_0-B** in **Fig. 9**; see also ref. [107]).

5. CONCLUSION AND OUTLOOK

The outcome of this work and of previous work on the S_2 state,[20,27-29,55-58,60,81] combined with further information, especially on substrate exchange rates,[13,14,108] has allowed a detailed picture of the first half of the catalytic cycle of the OEC to be developed. It is noted that this could only be achieved by the combination of experiments and theoretical model construction to provide essential selection constraints. In this way, EPR spectroscopy and DFT computations together yield a detailed, consistent picture of Mn oxidation states and ligand interactions of the OEC in the S_0 and S_2 states, the requirement for any mechanistic considerations. Here, the main results for the S_0 state comprise (i) the experimental characterization of the Mn1-His332-imino-N interaction, which in combination with EPR/^{55}Mn-ENDOR and DFT modeling enables the assignment of the oxidation states as $Mn1^{III}Mn2^{IV}Mn3^{III}Mn4^{III}$ and the site of oxygen bridge protonation as O5, as well as (ii) direct detection of an exchangeable oxygen bridge, identified as μO5-H. Its assignment as the first substrate is based on (i) the spectral similarities between S_0 and S_2 (**Fig. 6**), excluding any oxygen other than those ^{17}O sites observable in both these states, of which only O5 is bound to both the Ca^{2+} ion and Mn, as shown for W_s by mass spectrometry.[109] (ii) O5 is the only oxygen ligand being deprotonated during the transition from S_0 to S_1/S_2, consistent with the slowing of the W_s exchange.[13,14] This leads to the following reaction sequence (**Fig. 10**): (i) During the spontaneous transition from the transient state S_4 to S_0, the loss of four oxidation equivalents and release of O_2 are followed by the uptake of W_s, incorporated at the O5 position as a μ-hydroxo bridge, and release of a proton. (ii) The light-driven transition to S_1 proceeds most probably via oxidation of $Mn3^{III}$ to $Mn3^{IV}$ and release of the proton bound to O5 (see Refs. [3,34,39,108]). The proton-coupled electron transfer results in shortening of the $Mn4^{III}$-$Mn3^{IV}$ distance[42,43] and a significant decrease of the W_s exchange rate. (iii) Upon light-

induced oxidation of $Mn4^{III}$ to $Mn4^{IV}$ without release of a proton (see Refs. [3,36,108]), the Mn_4O_5Ca arrives at the structurally flexible[20] S_2 state, enabling faster W_s exchange. For completing our knowledge of the catalytic cycle, lacking the transitions to S_3 and S_4, which involve the most important process of O-O bond formation, the next step will be to extend our approach to obtain a more precise picture of the S_3 state than currently available,[22,110] including the proposed binding of the late substrate W_f using ^{17}O labeling.

ASSOCIATED CONTENT

PSII sample preparation; experimental details of the pulse EPR measurements; data processing: baseline correction and light-minus-dark subtraction; spectral simulations; theoretical background; multifrequency EPR and ^{55}Mn ENDOR spectra and simulations of the S_2 and S_0 states; the S_2 state: EPR/^{55}Mn ENDOR simulation parameters, Mn exchange couplings, fine structure interactions and spin projections; electronic structure of the S_0 state: spin projections, ^{55}Mn HFIs and Mn fine structure interactions; the Mn1–His332-imino-N interaction: field- and τ-dependent Q-band ^{14}N-three-pulse ESEEM and ^{14}N-HYSCORE experiments and interpretation of the simulation parameters; W-band ELDOR-detected NMR experiments; Interactions with exchangeable $^{1}H/^{2}H$ species: Q-band ^{2}H-three-pulse ESEEM and ^{2}H-HYSCORE experiments and simulations; general considerations on the experimental approach. This material is available free of charge via the Internet at http://pubs.acs.org.

AUTHOR INFORMATION

Corresponding Author

*E-mail: thomas.lohmiller@cec.mpg.de; nick.cox@anu.edu.au, nicholas.cox@cec.mpg.de.

Present Addresses

¶Department of Chemistry, University of Bath, Bath BA2 7AY, United Kingdom

Notes

The authors declare no competing financial interest.

ACKNOWLEDGMENT

We dedicate this work to Prof. Dr. Karl Wieghardt on the occasion of his 75th birthday. Financial support was provided by The Max-Planck-Gesellschaft, the "Bioénergie" program of the Commissariat à l'Énergie Atomique et aux Énergies Alternatives, the program FRISBI, the EU SOLAR-H2 initiative (FP7 contract 212508) and the Cluster of Excellence RESOLV (EXC 1069) funded by the Deutsche Forschungsgemeinschaft. T.L. was supported by the Federal Ministry of Education and Research of Germany (BMBF) in the framework of the Bio-H2 project (03SF0355C). A.W.R. is supported by the Royal Society (Wolfson Merit Award) and by BBSRC Research Grant BB/K002627/1. N.C. is supported by the Australian Research Council (Future Fellowship FT140100834).

REFERENCES

(1) Umena, Y.; Kawakami, K.; Shen, J.-R.; Kamiya, N. *Nature* **2011**, *473*, 55.
(2) Suga, M.; Akita, F.; Hirata, K.; Ueno, G.; Murakami, H.; Nakajima, Y.; Shimizu, T.; Yamashita, K.; Yamamoto, M.; Ago, H.; Shen, J.-R. *Nature* **2015**, *517*, 99.
(3) McEvoy, J. P.; Brudvig, G. W. *Chem. Rev.* **2006**, *106*, 4455.
(4) Cox, N.; Pantazis, D. A.; Neese, F.; Lubitz, W. *Acc. Chem. Res.* **2013**, *46*, 1588.
(5) Yano, J.; Yachandra, V. *Chem. Rev.* **2014**, *114*, 4175.
(6) Cox, N.; Pantazis, D. A.; Neese, F.; Lubitz, W. *Interface Focus* **2015**, 5.
(7) Krewald, V.; Retegan, M.; Pantazis, D. A. In *Solar Energy for Fuels*; Tüysüz, H., Chan, C. K., Eds.; Springer International Publishing: Cham, 2016, p 23.
(8) Pérez-Navarro, M.; Neese, F.; Lubitz, W.; Pantazis, D. A.; Cox, N. *Curr. Opin. Chem. Biol.* **2016**, *31*, 113.
(9) Joliot, P.; Barbieri, G.; Chabaud, R. *Photochem. Photobiol.* **1969**, *10*, 309.
(10) Diner, B. A.; Britt, R. D. In *Photosystem II: The Light-Driven Water:Plastoquinone Oxidoreductase*; Wydrzynski, T., Satoh, K., Eds.; Springer: Dordrecht, 2005; Vol. 1, p 207.
(11) Meyer, T. J.; Huynh, M. H. V.; Thorp, H. H. *Angew. Chem., Int. Ed.* **2007**, *46*, 5284.
(12) Kok, B.; Forbush, B.; McGloin, M. *Photochem. Photobiol.* **1970**, *11*.
(13) Hillier, W.; Wydrzynski, T. *Phys. Chem. Chem. Phys.* **2004**, *6*, 4882.
(14) Hillier, W.; Wydrzynski, T. *Coord. Chem. Rev.* **2008**, *252*, 306.
(15) Luber, S.; Rivalta, I.; Umena, Y.; Kawakami, K.; Shen, J. R.; Kamiya, N.; Brudvig, G. W.; Batista, V. S. *Biochemistry* **2011**, *50*, 6308.
(16) Grundmeier, A.; Dau, H. *Biochim. Biophys. Acta, Bioenerg.* **2012**, *1817*, 88.
(17) Galstyan, A.; Robertazzi, A.; Knapp, E. W. *J. Am. Chem. Soc.* **2012**, *134*, 7442.
(18) Kurashige, Y.; Chan, G. K. L.; Yanai, T. *Nat. Chem.* **2013**, *5*, 660.
(19) Vogt, L.; Ertem, M. Z.; Pal, R.; Brudvig, G. W.; Batista, V. S. *Biochemistry* **2015**, *54*, 820.
(20) Pantazis, D.; Ames, W.; Cox, N.; Lubitz, W.; Neese, F. *Angew. Chem., Int. Ed.* **2012**, *51*, 9935.
(21) Young, I. D.; Ibrahim, M.; Chatterjee, R.; Gul, S.; Fuller, F. D.; Koroidov, S.; Brewster, A. S.; Tran, R.; Alonso-Mori, R.; Kroll, T.; Michels-Clark, T.; Laksmono, H.; Sierra, R. G.; Stan, C. A.; Hussein, R.; Zhang, M.; Douthit, L.; Kubin, M.; de Lichtenberg, C.; Pham, L. V.; Nilsson, H.; Cheah, M. H.; Shevela, D.; Saracini, C.; Bean, M. A.; Seuffert, I.; Sokaras, D.; Weng, T. C.; Pastor, E.; Weninger, C.; Fransson, T.; Lassalle, L.; Brauer, P.; Aller, P.; Docker, P. T.; Andi, B.; Orville, A. M.; Glownia, J. M.; Nelson, S.; Sikorski, M.; Zhu, D. L.; Hunter, M. S.; Lane, T. J.; Aquila, A.; Koglin, J. E.; Robinson, J.; Liang, M. N.; Boutet, S.; Lyubimov, A. Y.; Uervirojnangkoorn, M.; Moriarty, N. W.; Liebschner, D.; Afonine, P. V.; Waterman, D. G.; Evans, G.; Wernet, P.; Dobbek, H.; Weis, W. I.; Brunger, A. T.; Zwart, P. H.; Adams, P. D.; Zouni, A.; Messinger, J.; Bergmann, U.; Sauter, N. K.; Kern, J.; Yachandra, V. K.; Yano, J. *Nature* **2016**, *540*, 453.
(22) Suga, M.; Akita, F.; Sugahara, M.; Kubo, M.; Nakajima, Y.; Nakane, T.; Yamashita, K.; Umena, Y.; Nakabayashi, M.; Yamane, T.; Nakano, T.; Suzuki, M.; Masuda, T.; Inoue, S.; Kimura, T.; Nomura, T.; Yonekura, S.; Yu, L. J.; Sakamoto, T.; Motomura, T.; Chen, J. H.; Kato, Y.; Noguchi, T.; Tono, K.; Joti, Y.; Kameshima, T.; Hatsui, T.;

Nango, E.; Tanaka, R.; Naitow, H.; Matsuura, Y.; Yamashita, A.; Yamamoto, M.; Nureki, O.; Yabashi, M.; Ishikawa, T.; Iwata, S.; Shen, J. R. *Nature* **2017**, *543*, 131.
(23) Styring, S.; Rutherford, A. W. *Biochemistry* **1987**, *26*, 2401.
(24) Messinger, J.; Renger, G. *Biochemistry* **1993**, *32*, 9379.
(25) Saito, K.; Rutherford, A. W.; Ishikita, H. *Proc. Natl. Acad. Sci. U. S. A.* **2013**, *110*, 7690.
(26) Askerka, M.; Vinyard, D. J.; Wang, J. M.; Brudvig, G. W.; Batista, V. S. *Biochemistry* **2015**, *54*, 1713.
(27) Rapatskiy, L.; Cox, N.; Savitsky, A.; Ames, W. M.; Sander, J.; Nowaczyk, M. M.; Rogner, M.; Boussac, A.; Neese, F.; Messinger, J.; Lubitz, W. *J. Am. Chem. Soc.* **2012**, *134*, 16619.
(28) Pérez Navarro, M.; Ames, W. M.; Nilsson, H.; Lohmiller, T.; Pantazis, D. A.; Rapatskiy, L.; Nowaczyk, M. M.; Neese, F.; Boussac, A.; Messinger, J.; Lubitz, W.; Cox, N. *Proc. Natl. Acad. Sci. U. S. A.* **2013**, *110*, 15561.
(29) Lohmiller, T.; Krewald, V.; Pérez Navarro, M.; Retegan, M.; Rapatskiy, L.; Nowaczyk, M. M.; Boussac, A.; Neese, F.; Lubitz, W.; Pantazis, D. A.; Cox, N. *Phys. Chem. Chem. Phys.* **2014**, *16*, 11877.
(30) Retegan, M.; Krewald, V.; Mamedov, F.; Neese, F.; Lubitz, W.; Cox, N.; Pantazis, D. A. *Chem. Sci.* **2016**, *7*, 72.
(31) Krewald, V.; Retegan, M.; Neese, F.; Lubitz, W.; Pantazis, D. A.; Cox, N. *Inorg. Chem.* **2016**, *55*, 488.
(32) Lavergne, J.; Junge, W. *Photosynth. Res.* **1993**, *38*, 279.
(33) Schlodder, E.; Witt, H. T. *J. Biol. Chem.* **1999**, *274*, 30387.
(34) Kulik, L. V.; Epel, B.; Lubitz, W.; Messinger, J. *J. Am. Chem. Soc.* **2007**, *129*, 13421.
(35) Siegbahn, P. E. M. *Acc. Chem. Res.* **2009**, *42*, 1871.
(36) Siegbahn, P. E. M. *Biochim. Biophys. Acta, Bioenerg.* **2013**, *1827*, 1003.
(37) Isobe, H.; Shoji, M.; Yamanaka, S.; Umena, Y.; Kawakami, K.; Kamiya, N.; Shen, J. R.; Yamaguchi, K. *Dalton Trans.* **2012**, *41*, 13727.
(38) Yamaguchi, K.; Yamanaka, S.; Isobe, H.; Saito, T.; Kanda, K.; Umena, Y.; Kawakami, K.; Shen, J. R.; Kamiya, N.; Okumura, M.; Nakamura, H.; Shoji, M.; Yoshioka, Y. *Int. J. Quantum Chem.* **2013**, *113*, 453.
(39) Pal, R.; Negre, C. F.; Vogt, L.; Pokhrel, R.; Ertem, M. Z.; Brudvig, G. W.; Batista, V. S. *Biochemistry* **2013**, *52*, 7703.
(40) Krewald, V.; Retegan, M.; Cox, N.; Messinger, J.; Lubitz, W.; DeBeer, S.; Neese, F.; Pantazis, D. A. *Chem. Sci.* **2015**, *6*, 1676.
(41) Saito, K.; Rutherford, A. W.; Ishikita, H. *Nat. Commun.* **2015**, *6*.
(42) Robblee, J. H.; Messinger, J.; Cinco, R. M.; McFarlane, K. L.; Fernandez, C.; Pizarro, S. A.; Sauer, K.; Yachandra, V. K. *J. Am. Chem. Soc.* **2002**, *124*, 7459.
(43) Haumann, M.; Müller, C.; Liebisch, P.; Iuzzolino, L.; Dittmer, J.; Grabolle, M.; Neisius, T.; Meyer-Klaucke, W.; Dau, H. *Biochemistry* **2005**, *44*, 1894.
(44) Sugiura, M.; Boussac, A.; Noguchi, T.; Rappaport, F. *Biochim. Biophys. Acta, Bioenerg.* **2008**, *1777*, 331.
(45) Sugiura, M.; Rappaport, F.; Brettel, K.; Noguchi, T.; Rutherford, A. W.; Boussac, A. *Biochemistry* **2004**, *43*, 13549.
(46) Boussac, A.; Rappaport, F.; Carrier, P.; Verbavatz, J. M.; Gobin, R.; Kirilovsky, D.; Rutherford, A. W.; Sugiura, M. *J. Biol. Chem.* **2004**, *279*, 22809.
(47) Ishida, N.; Sugiura, M.; Rappaport, F.; Lai, T. L.; Rutherford, A. W.; Boussac, A. *J. Biol. Chem.* **2008**, *283*, 13330.
(48) Reijerse, E.; Lendzian, F.; Isaacson, R.; Lubitz, W. *J. Magn. Reson.* **2012**, *214*, 237.
(49) Savitsky, A.; Grishin, Y.; Rakhmatullin, R.; Reijerse, E.; Lubitz, W. *Rev. Sci. Instrum.* **2013**, *84*.
(50) Nalepa, A.; Möbius, K.; Lubitz, W.; Savitsky, A. *J. Magn. Reson.* **2014**, *242*, 203.
(51) Cox, N.; Lubitz, W.; Savitsky, A. *Mol. Phys.* **2013**, *111*, 2788.
(52) Stoll, S.; Schweiger, A. *J. Magn. Reson.* **2006**, *178*, 42.
(53) Orio, M.; Pantazis, D. A.; Petrenko, T.; Neese, F. *Inorg. Chem.* **2009**, *48*, 7251.
(54) Pantazis, D. A.; Orio, M.; Petrenko, T.; Zein, S.; Bill, E.; Lubitz, W.; Messinger, J.; Neese, F. *Chem. Eur. J.* **2009**, *15*, 5108.
(55) Pantazis, D. A.; Orio, M.; Petrenko, T.; Zein, S.; Lubitz, W.; Messinger, J.; Neese, F. *Phys. Chem. Chem. Phys.* **2009**, *11*, 6788.
(56) Ames, W.; Pantazis, D. A.; Krewald, V.; Cox, N.; Messinger, J.; Lubitz, W.; Neese, F. *J. Am. Chem. Soc.* **2011**, *133*, 19743.
(57) Cox, N.; Rapatskiy, L.; Su, J.-H.; Pantazis, D. A.; Sugiura, M.; Kulik, L.; Dorlet, P.; Rutherford, A. W.; Neese, F.; Boussac, A.; Lubitz, W.; Messinger, J. *J. Am. Chem. Soc.* **2011**, *133*, 3635.
(58) Su, J. H.; Cox, N.; Ames, W.; Pantazis, D. A.; Rapatskiy, L.; Lohmiller, T.; Kulik, L. V.; Dorlet, P.; Rutherford, A. W.; Neese, F.; Boussac, A.; Lubitz, W.; Messinger, J. *Biochim. Biophys. Acta, Bioenerg.* **2011**, *1807*, 829.
(59) Krewald, V.; Neese, F.; Pantazis, D. A. *J. Am. Chem. Soc.* **2013**, *135*, 5726.
(60) Retegan, M.; Neese, F.; Pantazis, D. A. *J. Chem. Theory Comput.* **2013**, *9*, 3832.
(61) Staroverov, V. N.; Scuseria, G. E.; Tao, J.; Perdew, J. P. *J. Chem. Phys.* **2003**, *119*, 12129.
(62) Kossmann, S.; Kirchner, B.; Neese, F. *Mol. Phys.* **2007**, *105*, 2049.
(63) Jensen, K. P. *Inorg. Chem.* **2008**, *47*, 10357.
(64) Römelt, M.; Ye, S. F.; Neese, F. *Inorg. Chem.* **2009**, *48*, 784.
(65) Pantazis, D. A.; McGrady, J. E.; Maseras, F.; Etienne, M. *J. Chem. Theory Comput.* **2007**, *3*, 1329.
(66) Neese, F. *WIREs Comput. Mol. Sci.* **2012**, *2*, 73.
(67) van Lenthe, E.; Baerends, E. J.; Snijders, J. G. *J. Chem. Phys.* **1993**, *99*, 4597.
(68) van Lenthe, E.; Baerends, E. J.; Snijders, J. G. *J. Chem. Phys.* **1994**, *101*, 9783.
(69) Pantazis, D. A.; Chen, X. Y.; Landis, C. R.; Neese, F. *J. Chem. Theory Comput.* **2008**, *4*, 908.
(70) Schäfer, A.; Huber, C.; Ahlrichs, R. *J. Chem. Phys.* **1994**, *100*, 5829.
(71) Neese, F.; Wennmohs, F.; Hansen, A.; Becker, U. *Chem. Phys.* **2009**, *356*, 98.
(72) Weigend, F. *Phys. Chem. Chem. Phys.* **2006**, *8*, 1057.
(73) Klamt, A.; Schüürman, D. *J. Chem. Soc., Perkin Trans.* **1993**, 799.
(74) Messinger, J.; Nugent, J. H. A.; Evans, M. C. W. *Biochemistry* **1997**, *36*, 11055.
(75) Åhrling, K. A.; Peterson, S.; Styring, S. *Biochemistry* **1997**, *36*, 13148.
(76) Messinger, J.; Robblee, J. H.; Yu, W. O.; Sauer, K.; Yachandra, V. K.; Klein, M. P. *J. Am. Chem. Soc.* **1997**, *119*, 11349.

(77) Åhrling, K. A.; Peterson, S.; Styring, S. *Biochemistry* **1998**, *37*, 8115.
(78) Deák, Z.; Peterson, S.; Geijer, P.; Åhrling, K. A.; Styring, S. *Biochim. Biophys. Acta, Bioenerg.* **1999**, *1412*, 240.
(79) Kulik, L. V.; Epel, B.; Lubitz, W.; Messinger, J. *J. Am. Chem. Soc.* **2005**, *127*, 2392.
(80) Kulik, L. V.; Lubitz, W.; Messinger, J. *Biochemistry* **2005**, *44*, 9368.
(81) Lohmiller, T.; Ames, W.; Lubitz, W.; Cox, N.; Misra, S. K. *Appl. Magn. Reson.* **2013**, *44*, 691.
(82) Peloquin, J. M.; Campbell, K. A.; Randall, D. W.; Evanchik, M. A.; Pecoraro, V. L.; Armstrong, W. H.; Britt, R. D. *J. Am. Chem. Soc.* **2000**, *122*, 10926.
(83) Charlot, M.-F.; Boussac, A.; Blondin, G. *Biochim. Biophys. Acta, Bioenerg.* **2005**, *1708*, 120.
(84) Debus, R. J.; Campbell, K. A.; Gregor, W.; Li, Z. L.; Burnap, R. L.; Britt, R. D. *Biochemistry* **2001**, *40*, 3690.
(85) Yeagle, G. J.; Gilchrist, M. L.; McCarrick, R. M.; Britt, R. D. *Inorg. Chem.* **2008**, *47*, 1803.
(86) Yeagle, G. J.; Gilchrist, M. L.; Walker, L. M.; Debus, R. J.; Britt, R. D. *Phil. Trans. R. Soc. B* **2008**, *363*, 1157.
(87) Milikisiyants, S.; Chatterjee, R.; Weyers, A.; Meenaghan, A.; Coates, C.; Lakshmi, K. V. *J. Phys. Chem. B* **2010**, *114*, 10905.
(88) Stich, T. A.; Yeagle, G. J.; Service, R. J.; Debus, R. J.; Britt, R. D. *Biochemistry* **2011**, *50*, 7390.
(89) Zheng, M.; Khangulov, S. V.; Dismukes, G. C.; Barynin, V. V. *Inorg. Chem.* **1994**, *33*, 382.
(90) Schäfer, K. O.; Bittl, R.; Zweygart, W.; Lendzian, F.; Haselhorst, G.; Weyhermuller, T.; Wieghardt, K.; Lubitz, W. *J. Am. Chem. Soc.* **1998**, *120*, 13104.
(91) Sinnecker, S.; Neese, F.; Lubitz, W. *J. Biol. Inorg. Chem.* **2005**, *10*, 231.
(92) Stich, T. A.; Whittaker, J. W.; Britt, R. D. *J. Phys. Chem. B* **2010**, *114*, 14178.
(93) Chatterjee, R.; Milikisiyants, S.; Lakshmi, K. V. *Phys. Chem. Chem. Phys.* **2012**, *14*, 7090.
(94) Sinnecker, S.; Neese, F.; Noodleman, L.; Lubitz, W. *J. Am. Chem. Soc.* **2004**, *126*, 2613.
(95) Rapatskiy, L.; Ames, W. M.; Perez-Navarro, M.; Savitsky, A.; Griese, J. J.; Weyhermuller, T.; Shafaat, H. S.; Hogbom, M.; Neese, F.; Pantazis, D. A.; Cox, N. *J. Phys. Chem. B* **2015**, *119*, 13904.
(96) Aznar, C. P.; Britt, R. D. *Phil. Trans. R. Soc. B* **2002**, *357*, 1359.
(97) Britt, R. D.; Campbell, K. A.; Peloquin, J. M.; Gilchrist, M. L.; Aznar, C. P.; Dicus, M. M.; Robblee, J.; Messinger, J. *Biochim. Biophys. Acta, Bioenerg.* **2004**, *1655*, 158.
(98) Åhrling, K. A.; Evans, M. C. W.; Nugent, J. H. A.; Ball, R. J.; Pace, R. J. *Biochemistry* **2006**, *45*, 7069.
(99) Shafaat, H. S.; Griese, J. J.; Pantazis, D. A.; Roos, K.; Andersson, C. S.; Popovic-Bijelic, A.; Graslund, A.; Siegbahn, P. E. M.; Neese, F.; Lubitz, W.; Hogbom, M.; Cox, N. *J. Am. Chem. Soc.* **2014**, *136*, 13399.
(100) Soda, G.; Chiba, T. *J. Chem. Phys.* **1969**, *50*, 439.
(101) Soda, G.; Chiba, T. *J. Phys. Soc. Jpn.* **1969**, *26*, 249.
(102) Boussac, A.; Kuhl, H.; Ghibaudi, E.; Rogner, M.; Rutherford, A. W. *Biochemistry* **1999**, *38*, 11942.
(103) Tagore, R.; Crabtree, R. H.; Brudvig, G. W. *Inorg. Chem.* **2007**, *46*, 2193.
(104) Vinyard, D. J.; Khan, S.; Brudvig, G. W. *Faraday Discuss.* **2015**, *185*, 37.
(105) Tagore, R.; Chen, H. Y.; Crabtree, R. H.; Brudvig, G. W. *J. Am. Chem. Soc.* **2006**, *128*, 9457.
(106) Boussac, A.; Rutherford, A. W.; Sugiura, M. *Biochim. Biophys. Acta, Bioenerg.* **2015**, *1847*, 576.
(107) Paul, S.; Neese, F.; Pantazis, D. A. *Green Chem.* **2017**, *19*, 2309.
(108) Cox, N.; Messinger, J. *Biochim. Biophys. Acta, Bioenerg.* **2013**, *1827*, 1020.
(109) Hendry, G.; Wydrzynski, T. *Biochemistry* **2003**, *42*, 6209.
(110) Cox, N.; Retegan, M.; Neese, F.; Pantazis, D. A.; Boussac, A.; Lubitz, W. *Science* **2014**, *345*, 804.

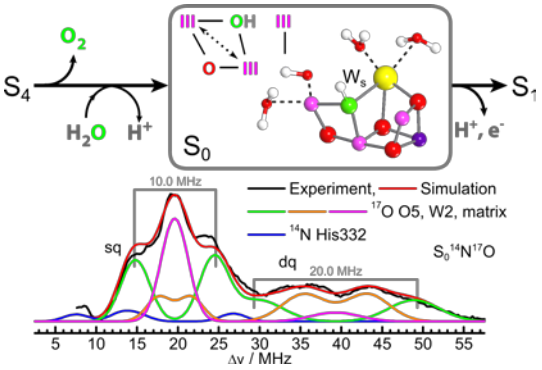

TOC Figure.